

**Measurement of the thulium ion spin Hamiltonian in an yttrium gallium garnet host crystal**Jacob H. Davidson,<sup>1</sup> Philip J. T. Woodburn,<sup>2</sup> Aaron D. Marsh,<sup>2</sup> Kyle J. Olson<sup>ⓧ</sup>,<sup>2</sup> Adam Olivera,<sup>2</sup> Antariksha Das<sup>ⓧ</sup>,<sup>1</sup> Mohsen Falamarzi Askarani,<sup>1</sup> Wolfgang Tittel,<sup>1,3,4</sup> Rufus L. Cone,<sup>2</sup> and Charles W. Thiel<sup>2</sup><sup>1</sup>*Qutech and Kavli Institute of Nanoscience, Delft University of Technology, 2628 CJ, Delft, The Netherlands*<sup>2</sup>*Department of Physics, Montana State University, Bozeman, Montana 59717, USA*<sup>3</sup>*Department of Applied Physics, University of Geneva, 1211 Geneva 4, Switzerland*<sup>4</sup>*Schaffhausen Institute of Technology–SIT, Geneva, Switzerland*

(Received 22 July 2021; revised 10 September 2021; accepted 13 September 2021; published 11 October 2021)

We characterize the magnetic properties for thulium ion energy levels in the  $\text{Y}_3\text{Ga}_5\text{O}_{12}$  (Tm:YGG) lattice with the goal to improve decoherence and reduce linewidth broadening caused by local host spins and crystal imperfections. More precisely, we measure hyperfine tensors for the lowest level of  $^3\text{H}_6$  and excited  $^3\text{H}_4$  states using a combination of spectral hole burning, absorption spectroscopy, and optically detected nuclear magnetic resonance. By rotating the sample through a series of angles with an applied external magnetic field, we measure and analyze the orientation dependence of the  $\text{Tm}^{3+}$  ion's spin Hamiltonian. Using this spin Hamiltonian, we propose a set of orientations to improve material properties that are important for light-matter interaction and quantum information applications. Our results yield several important external field directions: some to extend optical coherence times, another to improve spin inhomogeneous broadening, and yet another that maximizes mixing of the spin states for specific sets of ions, which allows improving optical pumping and creation of lambda systems in this material.

DOI: [10.1103/PhysRevB.104.134103](https://doi.org/10.1103/PhysRevB.104.134103)**I. INTRODUCTION**

Rare-earth-ion-doped crystals (REIC) have long been studied for use in high-frequency quantum and classical signal processing [1,2]. The transitions of interest are those between states of the  $4f^N$  configuration that are weakly permitted due to weak mixing with opposite parity states by the host crystal field. Additionally, these electrons are spatially isolated behind the  $5s$  and  $5p$  shell electrons that are distributed farther from the nucleus. These transitions have shown optical and spin coherence times of up to hundreds of microseconds and minutes, respectively, that enable interesting applications in quantum and classical data processing [3,4]. This coherence, and the associated applications, are often limited by time-varying electromagnetic fields in the local crystalline environment [5,6].

Trivalent thulium has received particular interest due to its simple energy level structure, long optical coherence time, and the availability of diode lasers at the 795-nm optical transition wavelength [7,8]. Of particular interest is  $\text{Tm}^{3+}$  embedded in yttrium gallium garnet ( $\text{Y}_3\text{Ga}_5\text{O}_{12}$ , Tm:YGG) for which optical coherence times ( $T_2$ ) on the order of milliseconds have recently been measured [9,10]. This ion and host crystal combination is still relatively unexplored compared to Tm:YAG. However, deeper understanding about the crystal dynamics, symmetry, and hyperfine structure has led to huge improvements in spectroscopic properties of optical and microwave transitions in other rare-earth-doped materials. One such example is the possibility of transitions with zero first-order Zeeman shifts (ZEFOZ), which may be obtained

by controlling the interplay of the measured terms of the ion's effective spin Hamiltonian, that can lead to orders of magnitude increase in spin coherence times [5]. Additionally, an effective spin Hamiltonian approximation can be used to improve and develop new experiments for applications of quantum networking and light matter interaction [11,12].

In this paper, we present a complete characterization of the hyperfine structure in the ground and excited states of the 795-nm optical transition of  $\text{Tm}^{3+}$  ions. To perform these measurements, we use absorption spectroscopy, spectral hole burning (SHB), and optically detected nuclear magnetic resonance (ODNMR) to isolate, measure, and confirm different terms of the effective spin Hamiltonian. These measurements individually produce information about the coupled behavior of these levels and the six magnetically equivalent, orientationally in-equivalent sites. Only by cross referencing the spectra from different sets of measurements are we able to decouple the information into the individual orientational behavior of each thulium ion in each individual site for each electronic level. Our results are then confirmed to be in good agreement with initial assumptions about crystalline structure [9] and a pair of independent measurements of the spin Hamiltonian terms using a single crystalline direction of Tm:YGG. This new knowledge allows us to predict the presence of optical clock transitions in this material that may allow extending the optical coherence times for light storage and quantum memory.

This paper is presented in the following order. In Sec. II, we give a brief overview of the Hamiltonian of the system and the remaining unknowns to be measured. In Sec. III, we

describe the general crystal geometry as well as the implications with regard to the Hamiltonian and how to isolate the specific projections of an external field on a specific ion site. Section IV describes the experimental setups used to produce the results. In Secs. V and VI, we describe how we gather spectra from hole burning and ODNMR measurements with different crystal orientations and which hyperfine tensor values stem from the results. Section VII contains details on a pair of independent measurements that confirm these tensor values for a specific orientation of the external field. In Sec. VIII, we discuss our results in the context of optical clock transitions and we identify a series of field orientations that may lead to improved optical coherence in this material.

## II. SPIN HAMILTONIAN FOR THE ENHANCED ZEEMAN AND QUADRATIC ZEEMAN EFFECTS

For a non-Kramers ion contained in a crystal lattice of low symmetry, a six-term Hamiltonian is often considered to describe the behavior of the ionic level structure [13,14].

$$H = (H_{\text{FI}} + H_{\text{CF}}) + H_{\text{HF}} + H_Q + H_{eZ} + H_{nZ}. \quad (1)$$

The first pair of terms describes the energy structure of a free ion ( $H_{\text{FI}}$ ) coupling to the local crystal field ( $H_{\text{CF}}$ ), which determines the energies of the states differentiated by total electron spin angular momentum that we are interested in for this work. The remaining four terms from contributions of the hyperfine ( $H_{\text{HF}}$ ), quadrupole ( $H_Q$ ), electronic Zeeman ( $H_{eZ}$ ), and nuclear Zeeman ( $H_{nZ}$ ) interactions are treated as small perturbations. The measurements conducted here focus on a specific pair of these electronic levels, specifically the lowest energy crystal field levels of the  $^3\text{H}_6$  and  $^3\text{H}_4$  multiplets. Additionally, the only isotope of thulium ( $^{169}\text{Tm}$ ) possesses a nuclear spin of  $1/2$  so that there is no nuclear quadrupole splitting and the  $H_Q$  term can be ignored [7,15,16].

The remaining terms of this Hamiltonian are magnetic in nature, corresponding to the hyperfine, electronic Zeeman, and nuclear Zeeman interactions. By expanding these remaining terms to second order as in Ref. [15], we arrive at a three term Hamiltonian,

$$H = \mathbf{B} \cdot (-g_n \beta_n \mathbb{I} - 2g_J \mu_B A_J \mathbf{\Lambda}_J) \cdot \mathbf{I} - g_J^2 \mu_B^2 \mathbf{B} \cdot \mathbf{\Lambda}_J \cdot \mathbf{B}, \quad (2)$$

where  $g_n$  is the nuclear gyromagnetic ratio of thulium,  $\beta_n$  is the nuclear magneton,  $g_J$  is electronic g factor for each level,  $\mu_B$  is the Bohr magneton,  $A_J$  is the hyperfine interaction constant,  $\mathbf{I}$  the ion's nuclear spin,  $\mathbf{B}$  the applied external field, and, finally,  $\mathbf{\Lambda}_J$  the hyperfine tensor. This tensor is given by second-order perturbation theory as

$$\Lambda_{J,(\alpha,\beta)} = \sum_{n \neq 0} \frac{\langle 0|J_\alpha|n\rangle \langle n|J_\beta|0\rangle}{E_n - E_0}, \quad \alpha, \beta \in \{x, y, z\} \quad (3)$$

where  $\langle 0|J_\alpha|n\rangle$ ,  $\langle n|J_\beta|0\rangle$  are wave-function matrix elements for the electronic levels of interest, and the sum is over the crystal field levels with energies  $E_n$  [7,15,16].

The first two terms in Eq. (2) describe the enhanced effective nuclear Zeeman effect that results from the second-order coupling of the hyperfine interaction between the electronic Zeeman effect and the first-order nuclear Zeeman interaction.

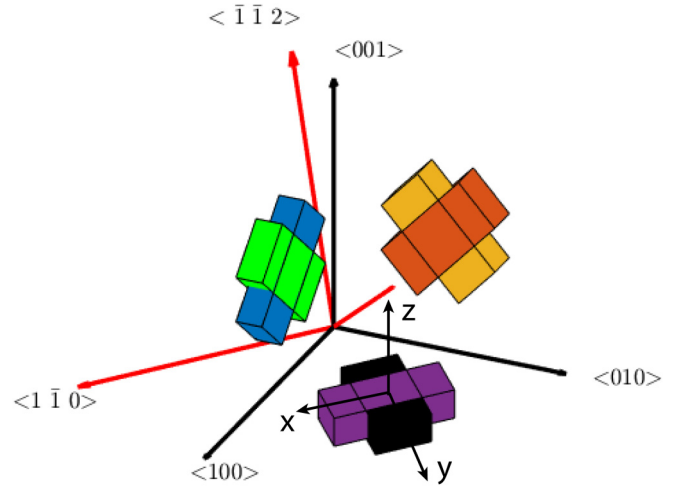


FIG. 1. Possible sites of  $\text{Tm}^{3+}$  ions in a YGG crystal. Black thick axes denote the cubic unit cell boundaries. Each of the six colored cuboids denotes the location as well as the direction of the ion's local  $Y$  axis (along the cuboids largest dimension), that is also expected to be the direction of the optical transition dipole moment of the thulium transition, relative to a cubic crystal cell. Each site is identified by a specific color throughout the remainder of this paper: “site 1” (black), “site 2” (purple), “site 3” (orange), “site 4” (yellow), “site 5” (green), and “site 6” (blue). Red axes denote the symmetry axes along which the crystal is grown and oriented for these studies. Throughout this paper, we will characterize rotations with respect to these directions  $\langle 1\bar{1}0 \rangle$ ,  $\langle 111 \rangle$ ,  $\langle \bar{1}\bar{1}2 \rangle$ . Finally, the labeled  $(x, y, z)$  thin black axes denote the local site axes as defined by the  $D_2$  point group symmetry (shown for the example of site 1).

The third term is the quadratic Zeeman effect that results from the expansion of the electronic Zeeman term where the orientation dependence is again determined by a scaled version of the same hyperfine tensor,  $\mathbf{\Lambda}$  [17]. Other terms that arise from the expansion to second order are small and neglected. With this description in place, the only unknowns in Eq. (2) are the 18 matrix elements of the hyperfine tensors  $\mathbf{\Lambda}_{g,e}$ , with each a  $3 \times 3$  matrix that describes the magnetic interactions of these levels for  $\text{Tm}^{3+}$  ions in this material. The level structure with an applied magnetic field is shown in Fig. 2(a). The effect of the quadratic term can be seen as a shift of the whole electronic crystal field level, and the linear term [Fig. 2(a), inset] splits the pair of nuclear spin states. The number of unknown elements in this tensor drops further due to the local symmetry of the  $\text{Tm}^{3+}$  ions that occupy yttrium in the YGG lattice.

## III. CRYSTAL SYMMETRY AND SITE SELECTION

The location and symmetry of the yttrium sites is well understood for garnet crystals [3,18,19]. YGG is a cubic crystal with space group symmetry  $O_h^{10}$ , and the thulium sites feature  $D_2$  point group symmetry [9]. The site symmetry, as described for the similar case of  $\text{Tm}:\text{YAG}$  [20] and depicted in Fig. 1, allows for six crystallographically equivalent yet orientationally inequivalent substitution sites.

The magnetic behavior of  $\text{Tm}^{3+}$  in each of these sites is the same, due to the ion being locally surrounded by the same

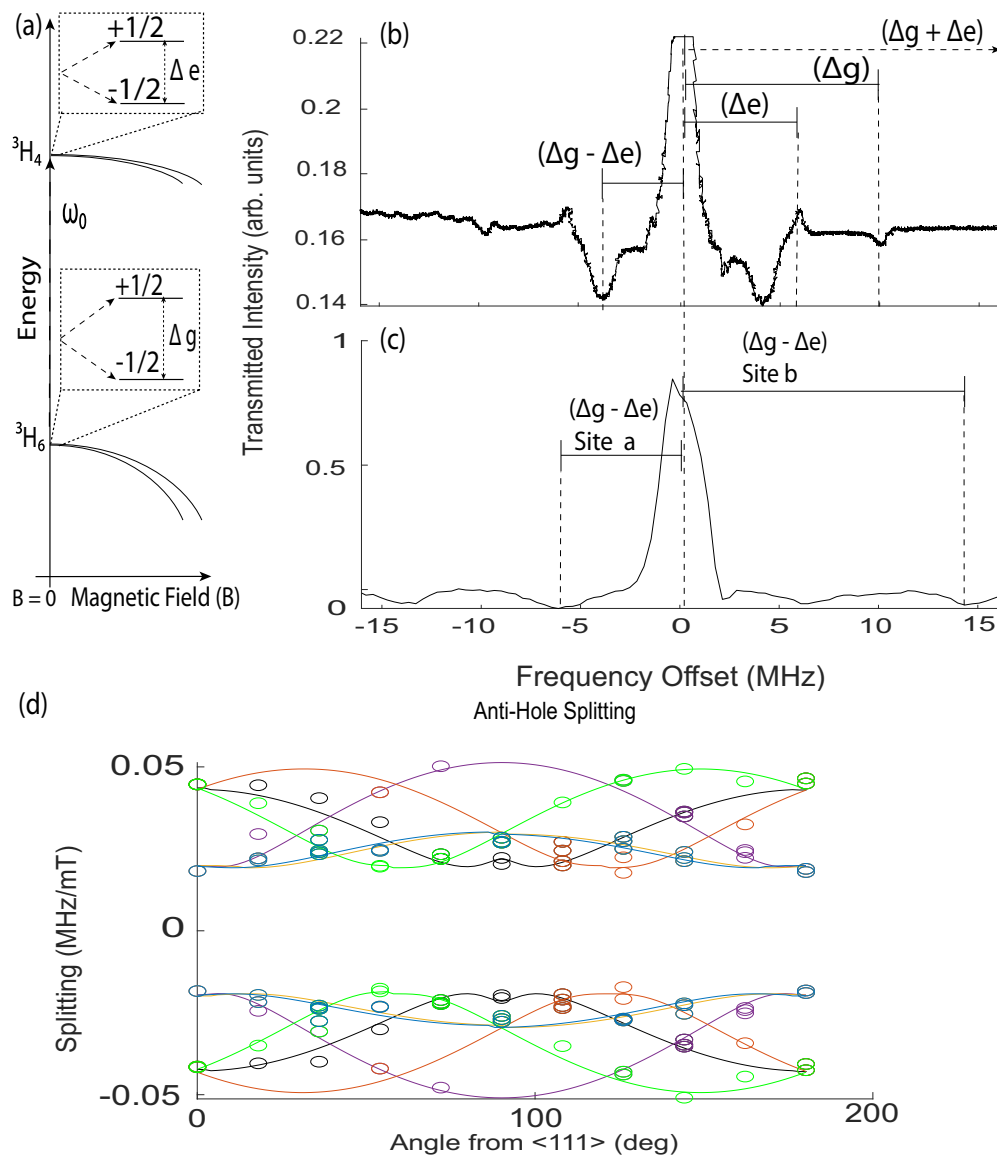


FIG. 2. (a) Diagram of the level structure for the optical transition in  $^{169}\text{Tm}_{3+}$  with increasing magnetic field. Note that on a large scale, the change in energy of all the states is dominated by the quadratic term, but for small fields it is linear. (b) A detailed serrrodyne scan of a spectral hole structure measured for a magnetic field of 90 mT applied along the crystalline  $\langle 111 \rangle$  axis. The small spectral feature at  $\sim 2$  MHz likely arises from the only other set of sites for this orientation. (c) Double passed AOM frequency scan of a broader spectral hole at 300 mT. Only  $\Delta_g - \Delta_e$  antiholes are visible for a pair of differently oriented sites. (d) Markers show the antihole frequencies plotted vs the angle between the external magnetic field and the crystal's  $\langle 111 \rangle$  axis. Solid lines of each color are fits of a “difference” tensor to each of the six potential sites for the ions with a correlation coefficient  $R^2 > 90\%$ .

structural and chemical environment. However, the ion and its local environment occurs with six different orientations with respect to the cubic crystal cells of the garnet, leading to orientational, and in essence magnetic, in-equivalence between the sites. Here, as in Ref. [20] and Fig. 1, there are specific directions with respect to the cubic crystal axes that cast different subsets of the orientationally in-equivalent sites into classes of ions that share the same projections of applied electromagnetic fields ( $\vec{E}$ ,  $\vec{B}$ ) onto the local  $\text{Tm}^{3+}$  site axes. For fields ( $\vec{E}$ ,  $\vec{B}$ ) directed along the crystalline  $\langle 111 \rangle$  and  $\langle 001 \rangle$  sets of directions ( $\langle 110 \rangle$ ,  $\langle \bar{1}\bar{1}2 \rangle$  and  $\langle 100 \rangle$ ,  $\langle 010 \rangle$ , respectively). These symmetric directions serve as a labeling convention for growth, dicing, and orientation of

these crystals and are built into the models detailed below, which allows us to determine the relative projection of incident fields on each of the  $\text{Tm}^{3+}$  ion sites throughout our experiments.

On a more microscopic level, the local  $D_2$  symmetry for each site is such that, by using a set of axes around the  $\text{Tm}^{3+}$  ion defined by that site symmetry, we can diagonalize the hyperfine tensor from Sec. II. This leaves only the six diagonal elements,  $\Lambda_{J,(x,y,z)}$  (three for each electronic state  $J$ ), which correspond to the tensor elements along the three axes shown in Fig. 1 for “site 1” of the six sites. Considering the crystal symmetry, the entire enhanced effective Zeeman term of Eq. (2) for a given electronic level can be simplified

to [7,16]

$$H_{J,(x,y,z)} = -\hbar\sqrt{g_{J,x}^2 B_x^2 + g_{J,y}^2 B_y^2 + g_{J,z}^2 B_z^2} \cdot \mathbf{I} \quad (4)$$

for

$$g_{J,(x,y,z)} = -g_n \beta_n - 2g_J \mu_B A_J \Lambda_{J,(x,y,z)}. \quad (5)$$

The determination of the six remaining parameters (three per electronic level) will be discussed in later sections. To measure these parameters, we gather data on the splittings of the ground and excited hyperfine states for a series of different orientations of a Tm:YGG crystal sample. In spherical coordinates, each specific orientation  $(\theta, \phi)$  relative to the cubic crystal cell shown in Fig. 1 has a fixed set of projections on each of the six potential  $\text{Tm}^{3+}$  ion site axes. Thus, for every angle of the magnetic field with a macroscopic, oriented sample, we can determine from the expected geometry the exact magnetic projection on each  $\text{Tm}^{3+}$  ion axis. By matching sets of these magnetic field projections to various measurements of the hyperfine splitting we determine the desired hyperfine tensor values.

#### IV. EXPERIMENTAL SETUP

To gather the data for our study, we used a total of five Tm:YGG crystals, each one cut along the symmetric dimensions of the cubic crystal cell. In addition, we employed several experimental setups. While similar in concept (laser  $\rightarrow$  pulsing  $\rightarrow$  frequency control  $\rightarrow$  cold crystal in a magnetic field  $\rightarrow$  detector), they featured technological differences. For example, we used different cryogenic systems—two helium flow cryostats reaching a base temperature of  $< 2$  K, equipped with magnets that allow applying fields of up to 7 T and fitted with a gearing system that allows rotating the cooled sample by up to  $360^\circ$  around a fixed optical axis for each crystal sample; and an adiabatic demagnetization refrigerator reaching 500 mK temperature, equipped with a 2-T magnet as well as a static crystal holder.

To address the center of the inhomogeneously broadened  ${}^3\text{H}_6 \leftrightarrow {}^3\text{H}_4$  optical transition of thulium at 795.325-nm wavelength, we used either a titanium sapphire laser or an external cavity diode laser. The light was subsequently directed through an acousto-optic modulator (AOM), which allowed creating pulses out of the continuous-wave laser light. Additionally, we used either an AOM in double-pass configuration, or a phase modulator driven by a serrrodyne signal, to frequency modulate the light. The appropriately prepared pulses were then directed to the cooled Tm:YGG samples either by free space or by using a single-mode optical fiber. The beam diameter inside the samples were around  $500 \mu\text{m}$  in case of the flow cryostat and free-space coupling, and around  $200 \mu\text{m}$  in the other case. Finally, the light was sent into a photodetector, and the electrical signals were displayed on an oscilloscope and recorded for analysis.

The set of ODNMR experiments detailed in Sec. VI also required the application of radio-frequency signals that vary between 20 kHz and 10 MHz. Towards this end, one of the flow cryostats is equipped with an impedance matched copper coil that provides an adjustable frequency RF field around the crystal sample. This coil is driven using 5–10 W RF power,

created by means of a RF signal generator, a pair of 40-dB amplifiers, as well as variable attenuation. For each frequency, the output from the signal generator was set to the desired value and mixed with RF noise, low passed to 100 kHz before being sent to the coil, and terminated to  $50 \Omega$ . The added noise increases the RF tone bandwidth to provide an RF field capable of driving a larger population of spins, and in turn create signals with higher SNR.

Additional information about the experimental setups will be given in Secs. V–VII along with the description of the measurements.

#### V. SPECTRAL HOLE BURNING DESCRIPTION AND RESULTS

The six unknown tensor values appear in both the linear and quadratic terms of the Hamiltonian such that measurements of either term's orientation dependence is sufficient to determine the entire spin-Hamiltonian. The linear splitting of hyperfine levels the ground and excited states can be observed through spectral hole burning measurements [13]. With a magnetic field applied, both the ground and excited electronic states split into spin up  $+\frac{1}{2}$ , ( $|\uparrow\rangle$ ) and spin down  $-\frac{1}{2}$ , ( $|\downarrow\rangle$ ) states, creating a pair of levels seen in Fig. 2(a) (inset). Even at cryogenic temperatures, both ground-state spin states are equally populated. Spectral hole burning drives atomic population through this level structure, resulting in long lasting population differences between the different spin states [8]. The details of this optical pumping mechanism are well understood and are detailed in Refs. [21,22]. The initial pump pulse creates the main spectral hole: a reduction of the atomic absorption of the ensemble at the chosen pulse frequency within the in-homogeneous broadening of the crystal.

Considering only a single projection of the magnetic field on a site, ions in the selected bandwidth are pumped to the other ground-state hyperfine level and thereby create a feature with increased absorption, referred to as an antihole, at a frequency offset given by the ground-state splitting,  $\Delta_g$ . Due to the inhomogeneously broadened nature of the transition, additional antiholes and a single side hole arise symmetrically around the main hole at frequency offsets of  $(\Delta_g \pm \Delta_e)$  and  $\Delta_e$ , respectively. By frequency sweeping weak laser light over the spectral region surrounding the main hole and recording the transmitted intensity, these population differences are visible as shown in Fig. 2(b). By measuring the frequency offset of side and antiholes for a set of different orientations we can determine the hyperfine tensor in Eq. (2).

For an arbitrary orientation, each site has a different projection of the external field on its local axes. Thus, based on that projection, it is possible that the same spectral feature (e.g., the first antihole at  $\Delta_g - \Delta_e$ ) from separate sites may be visible at different frequencies. In the worst case, this could result in crowded spectra that contain as many as 48 features that would need to be assigned to different sites and associated external field projections. Fortunately, due to the fixed orientations of the sites with respect to the symmetric crystal axes, some orientations cast sites into equivalent subsets, making their spectral features appear at the same frequencies. This is the case in Fig. 2(b) where the visible features belong to three different sites 1, 3, and 5 that all

share the same field projection. However, for a different case of Fig. 2(c), the visible features show only the  $(\Delta g - \Delta e)$  antiholes for a pair of  $\text{Tm}^{3+}$  sites with different magnetic field projections. Thus, with hole spectra from a series of different orientations, the problem then becomes interpreting each spectrum and making an assignment for each feature to a particular site and its corresponding external field projection. This process provides us with a set of splittings that can be used to determine the tensor values for a given site at a given orientation.

This experiment was conducted in one of the flow cryostats described in Sec. III. The  $\text{Tm}:\text{YGG}$  sample was cooled to 2 K and a fixed field of 300 mT was applied as the sample was rotated through a series of angles. To create a hole spectrum, the experimental burning sequence at each angle involved a 1 ms hole burning pulse, a waiting period of 10 ms for population to decay from the excited state, and finally a  $100 \mu\text{s}$  read pulse with a frequency chirped over a 40-MHz region centered at the main hole to reveal any side and antihole structure. This sequence used circularly polarized light with  $\sim 10$  mW of power incident on the crystal and was averaged over dozens of scans to produce a single spectrum at each angle. Due to a combination of pump laser linewidth, sample temperature, and limited AOM frequency shifting efficiency, we were only able to monitor and record the frequency change of the first antihole, occurring at a frequency offset of  $(\Delta g - \Delta e)$ , for all sites during these rotational SHB measurements.

Though not a direct measurement of the tensor values of either the ground or excited state, these values contain information that in conjunction, with the ODNMR data from Sec. V, is used to compute the spin-Hamiltonian. Tracking these splittings through the series of different angles between an external magnetic field and the symmetric crystal axes, we define a ‘‘difference tensor’’ that best satisfies the measured  $(\Delta g - \Delta e)$  splittings for all sites at all angles.

More specifically, for a specific angle of external field with respect to a particular crystal direction, there is a known projection of the magnetic field on each of the six sites. Our fitting procedure fits  $g_{(x,y,z)}$  values in Eq. (4) to a particular splitting that is assigned to a site and determines the three associated magnetic field projections ( $B_x, B_y, B_z$ ) at each angle. Thus one set of fitted values match an entire matrix of magnetic projections for a series of angles with regard to each site to a set of splitting values assigned to each site. The spectral locations of the visible antiholes at the series of angles compared to the results of this least squares tensor fitting procedure can be seen in Fig. 2(d). This fitting procedure and analysis were repeated for two differently oriented  $\text{Tm}:\text{YGG}$  crystals, and good agreement was found between the resulting ‘‘difference tensors.’’ For more information regarding the fitting procedure, and plots of the fit for the second crystalline direction, consult Ref. [23].

## VI. ODNMR MEASUREMENT AND RESULTS

In addition to SHB, where optical pumping drives changes in hyperfine level population by way of the optical excitation to the excited state followed by spontaneous relaxation, it is also possible to alter the relative hyperfine level populations by directly addressing the microwave transition between

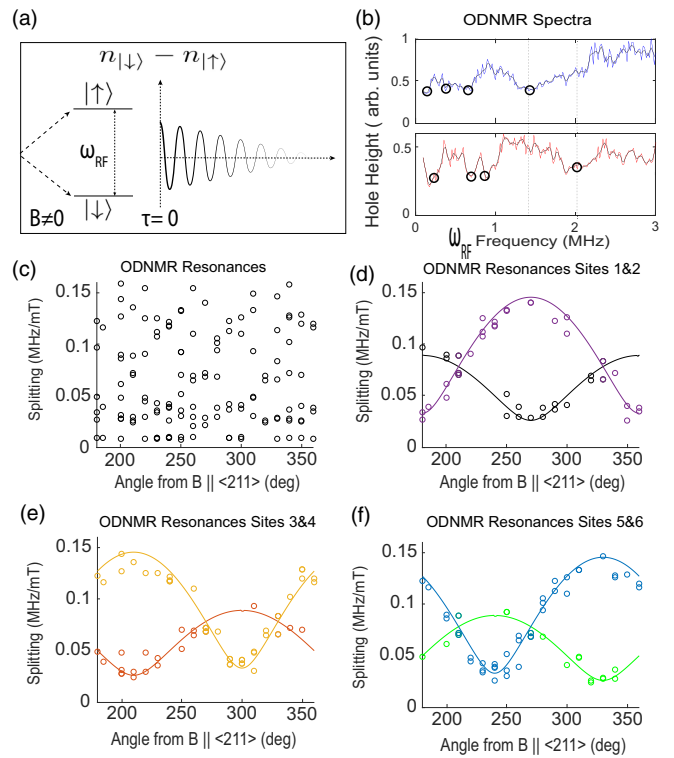


FIG. 3. (a) Diagrammatic view of the ODNMR experiment, including the driven spin transition that appears at small magnetic fields, and the coherent RF drive that equalizes the population between the  $\pm\frac{1}{2}$  spin states. (b) The  $\omega_{\text{RF}}$  frequencies that diminish the height of a spectral hole are identified as resonances by a smoothing and peak finding algorithm and then confirmed manually. The top trace shows these resonances with an applied external field of 22.4 mT, while the lower trace and dotted lines show the shift of a marked feature for an increased field of 31.4 mT. A spectrum similar to these, each with unique resonance frequencies, is generated for many angles of the external field relative to the crystal orientation. (c) A plot of resonances from all spectra at a series of angles between external field and the crystal  $\langle 211 \rangle$  direction. [(d)–(f)] Site by site fitting of the tensors listed in Table I to the resonances from (c) across a series of angles.

them. The relative population between the hyperfine levels can then be observed optically in a double resonance experiment known as optically detected nuclear magnetic resonance, which has been carried out with a number of REICs [13,24,25]. As opposed to SHB, ODNMR provides information directly about either  $\Delta g$  or  $\Delta e$  and thereby supplements the results in the previous section to extract the Hamiltonian in Eq. (2). This approach, shown in Fig. 3(a), involves first creating a population difference between the hyperfine levels via SHB. While viewing this hole profile optically, an RF pulse is applied that, if resonant with the spin transition at frequency  $\Delta g$ , partially re-equalizes the population, resulting in a change of the absorption depth of the spectral hole. Since the energy difference between hyperfine states is unknown for a given external magnetic field the RF field is swept across a range of frequencies to find the resonance condition  $\omega_{\text{RF}} = \Delta g$ . The excited state splitting  $\Delta e$  can be measured with a similar approach using an altered sequence of optical and RF

TABLE I. Spin Hamiltonian values. The  $g_j$  values are calculated using the general formalism described in Ref. [14]. The  $A_j$  values are from Ref. [7] and can be recalculated from Ref. [14] as they depend only on the expectation value for electron radius for this  $\text{Tm}^{3+}$  transition. The  $g_{x,y,z}$  values for the excited and ground states are measured in this work. Together with the listed constants, they allow calculating all  $\Lambda_{J,\alpha}$  values using Eq. (5).

|                | $^3\text{H}_6(\text{g})$ | $^3\text{H}_4(\text{e})$ |
|----------------|--------------------------|--------------------------|
| $g_n\beta_n$   | $-3.53$ (MHz/T)          | $-3.53$ (MHz/T) [27]     |
| $g_j$          | 1.16                     | 0.8                      |
| $A_j$          | $-470.3$ (MHz)           | $-678.3$ (MHz)           |
| $A_j\Lambda_x$ | $-7.23 \times 10^{-4}$   | $-1.55 \times 10^{-4}$   |
| $A_j\Lambda_y$ | $-4.47 \times 10^{-3}$   | $-3.95 \times 10^{-3}$   |
| $A_j\Lambda_z$ | $-9.99 \times 10^{-4}$   | $-5.57 \times 10^{-4}$   |
| $g_x$          | $27 \pm 1.7$ (MHz/T)     | $7 \pm 2.5$ (MHz/T)      |
| $g_y$          | $146 \pm 1.5$ (MHz/T)    | $92 \pm 2.8$ (MHz/T)     |
| $g_z$          | $36 \pm 2.6$ (MHz/T)     | $16 \pm 3.1$ (MHz/T)     |

excitation pulses such that population can be addressed and probed while in the excited state.

This experiment was carried out in one of the helium flow cryostats, equipped with an RF coil on a rotation mount to apply the RF fields. The  $\text{Tm}:\text{YGG}$  sample is cooled to 2 K and an external magnetic field of 20–40 mT is applied perpendicular to the optical and rotational axis along the crystalline  $\langle 211 \rangle$  direction. Using an altered SHB experimental sequence, a spectral hole is prepared and read out, with burning and waiting times adjusted to ensure minimal contribution to the spectral hole depth from atomic population in the excited states while maximizing the repetition rate. Additionally, the duration and relative powers of the burn and read pulses were adjusted to produce a slightly shallower hole that could be read with less noise caused by laser power fluctuations.

While repeating the hole burning experiment, 100-ms-long RF pulses are applied to the crystal. We tuned the frequency of the RF field in 20 kHz steps from 100 kHz–4 MHz and five repetitions are averaged to produce spectra as seen in Fig. 3(b). The broadening of the features is due to the convolution of the applied RF field linewidth of 100 kHz and the RF resonance in-homogeneous linewidth. To ensure that these features showed the ground-state resonances, we first confirmed that each resonance frequency had a linear shift with increasing external magnetic field and were absent when no external field was applied. We optimized the generation of the ODNMR spectra over the parameter space of RF drive power, optical hole burning power, duration, sample temperature, SHB duty cycle, and experimental repetition rate to produce the best signal to noise ratio for these resonance scans.

This experiment was repeated for a series of different angles between the crystal  $\langle 211 \rangle$  axis and the externally applied magnetic field. All resonance frequencies were determined with help of a peak finding algorithm, and are displayed in Fig. 3(c). As before, all six Tm sites contribute to this set of resonances.

Here again, each specific angle of external field with respect to a particular crystalline direction defines six projections of the magnetic field on each site. Each angle is

associated with a series of ODNMR resonances as well, such that a vector of ground-state tensor values must solve, as closely as possible, a matrix equation that includes magnetic projections on each site for many local angles, to fit over more than 200 equally weighted resonance points. The resulting tensor fits are shown in Figs. 3(d)–3(f). Site assignment and fitting was repeated for two differently oriented  $\text{Tm}:\text{YGG}$  crystals that show good agreement with one another. The results of the second fit can be seen in Ref. [23]. It is interesting to note that the calculated tensor values are comparable to those measured with  $\text{TmGG}$  [26]. This gives us additional confidence in the results, as in the case of the confirmation between  $\text{Tm}:\text{YAG}$  and  $\text{TmAG}$  [22,27].

This fitting procedure produces the three ground-state tensor values  $\Lambda_{g,(x,y,z)}$ , and in conjunction with the “difference tensor” fits from the previous section,  $\Lambda_{e,(x,y,z)}$  can also be determined. These results for the six spin-Hamiltonian components averaged over the four directional fits of Secs. V and VI are shown in Table I, where the signs are given by convention. Unfortunately, both spectral hole burning and ODNMR yield only the magnitude but not the sign of the different parameters because we cannot differentiate one hyperfine state from another. Nonetheless, and similarly to Ref. [28], for our purposes, it is often enough to know the relative energy difference between the two hyperfine states of each electronic level, and not whether it happens to be the spin up or spin down state since their energy shifts will be symmetric.

## VII. VERIFICATION OF RESULTS

In the following, we detail additional measurements based on alternative methods and on different  $\text{Tm}:\text{YGG}$  crystals. While being performed with a reduced set of parameters that does not allow independently establishing the Hamiltonian in Eq. (2), they nevertheless allow verifying the results presented in Sec. VI.

### A. Linear Zeeman shift

The enhanced effective Zeeman interaction given by the first two terms of Eq. (2) results in a linear splitting of the hyperfine levels in both the ground and excited states. As discussed in Sec. IV, the Zeeman coefficient can be measured by first applying a magnetic field, then exposing the sample to narrow-band laser light, and finally probing the resulting sequence of holes and antiholes by frequency scanning a weak laser across the created spectral features.

This experiment was performed inside the ADR and at a temperature of 500 mK. In this case, the magnetic field could only be applied along the crystal’s  $\langle 111 \rangle$  direction, resulting in magnetic projections of equal magnitude on the Y and Z components of sites 1,3, and 5, and the X and Z components of sites 2, 4, and 6. The holeburning laser was frequency locked to around 10-kHz linewidth by means of a stable optical reference cavity and the Pound-Drever-Hall method, and we employed 1 mW of power incident on the crystal, burning pulses of 200 ms duration, 10 ms of waiting time to avoid spontaneously emitted signal, and a 1-ms-long read pulse. The lower temperature and narrower laser linewidth (compared to the measurements described before) allowed resolving all

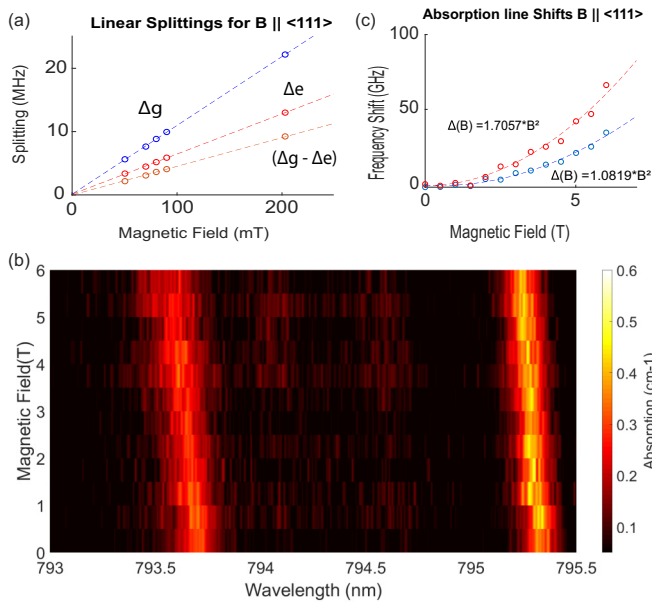


FIG. 4. (a) The linear splitting of the antiholes shown in Fig. 2(b) for the  $B \parallel \langle 111 \rangle$  orientation yields values of 45 and  $108 \pm 2$  MHz/T and a side hole splitting of  $63 \pm 2$  MHz/T. (b) Absolute absorption frequency for the optical transitions from the lowest ground-state crystal field level to the first (795.325 nm) and second (793.7nm) excited state crystal field levels with increasing magnetic field. (c) A closer look at the behavior of these transitions reveals the expected quadratic nature of the frequency shift.

expected SHB features, including a pair of anti holes and a side hole, as seen in Fig. 2(b) for a field of 90 mT.

The splitting of these spectral features as a function of magnetic field shown in Fig. 4(a) confirms the linear nature of the Zeeman interaction with splittings of the ground and excited states of  $108 \pm 2$  and  $63 \pm 2$  MHz/T, respectively. This is in good agreement with the values calculated from the measured tensors, which we found to be  $\Delta_g = 106 \pm 2.2$  MHz/T,  $\Delta_e = 66 \pm 1.3$  MHz/T for sites 1,3, and 5 at this orientation.

### B. Quadratic Zeeman shift

The quadratic Zeeman interaction given by the third term of Eq. (2) shifts each electronic crystal field level, characterized by the total angular momentum  $J$ , parabolically due to the so-called VanVleck paramagnetism [29]. Each crystal field level shifts with its own rate, as depicted in Fig. 2(a) and described by its hyperfine tensor. This creates an overall shift of the optical transition frequency with a  $B^2$  dependence that varies based on the external field direction. It can be calculated using the ground-state and excited-state tensor values given in Table I.

To measure the quadratic Zeeman effect, we used a flow cryostat operating at 5 K with an applied magnetic field along the  $\langle 111 \rangle$  direction of the Tm:YGG crystal. We performed white light absorption spectroscopy, similar to Ref. [16], i.e., we directed collimated CW white light through the crystal and to an optical spectrum analyzer to observe the entire inhomogeneous line of the  ${}^3\text{H}_6 \leftrightarrow {}^3\text{H}_4$  transition at 795.325 nm [see Fig. 4(b)]. The optical transition from lowest crystal field

level of the ground state to the second crystal field level of the excited state at 793.7 nm was visible as well, confirming the expected crystal field spacing of  $26 \text{ cm}^{-1}$  in Ref. [3]. We monitored the absorption frequencies for this pair of transitions as the external magnetic field was increased from 0 to 6 T. The results are depicted in Fig. 4(c). A quadratic fit yields a frequency shift of  $\Delta = 1.08 \pm 0.24 \text{ GHz/T}^2$ , which is in good agreement with the value of  $\Delta_p = 1.09 \pm 0.25 \text{ GHz/T}^2$  that we calculated from the measured hyperfine tensors.

## VIII. OPTICAL CLOCK TRANSITIONS AND SPECIAL DIRECTIONS

The frequency of the transition between two hyperfine states—one belonging to the electronic ground state and one of the excited state—depends on the applied magnetic field through the linear and quadratic Zeeman effects. Small field fluctuations therefore cause spectral diffusion and hence a reduction of the optical coherence time. It is sometimes possible to choose a magnetic field magnitude and a crystal orientation for which the transition energy becomes, to first order, insensitive to fluctuations in the magnetic field. These transitions are referred to as optical clock transition and are analogous to the ZEFOZ transitions from Refs. [5,28,30,31]. Clock transitions are extremely powerful tools used for reducing decoherence due to noisy magnetic fields [32]. These clock transitions exist in Tm:YGG and can be found for a particular site using the procedure detailed below.

Inspecting the third term of Eq. (2) and taking into account that the elements of the hyperfine tensor  $\Gamma_J$  are larger in the ground state than in the excited state (see Ref. [16] for a detailed explanation in Tm:YAG) the optical transition energy change caused by the quadratic Zeeman effect creates an increase in transition energy with magnetic field. This is depicted theoretically in Fig. 2(a) and confirmed from the data in Fig. 4(b).

Furthermore, looking at the first and second terms of Eq. (2), which describe the linear Zeeman shift, we find that there exist ground and excited state pairs of hyperfine states for which the optical transition frequency decreases with applied magnetic field. Hence, for certain combinations of crystal orientation (or rather orientation of a local Tm<sup>3+</sup> site) with respect to the magnetic field, magnetic field strength and spin values, the linear and quadratic Zeeman effects oppose each other, and an optical clock transition can be observed [33]. This transition must have a field magnitude insensitive point, which is shown in Fig. 5(a) as the shift in optical transition frequency  $\Delta E_{\text{opt}}(|B|, \theta, \phi)$  versus applied field magnitude.

In these cases, the spin-Hamiltonian terms form a quadratic function that must have an extremum, i.e., a field-magnitude-insensitive point, at some positive field magnitude. The first condition of an optical clock transition, a field magnitude  $|B|$  such that  $\frac{\partial \Delta E_{\text{opt}}}{\partial |B|} = 0$ , is calculated for every orientation of magnetic field relative to the “site 1” spin -1/2 conserving optical transition in Fig. 5(b) using a mesh size of 1mT and 1 degree angular steps.

For the remaining angular derivatives ( $\frac{\partial \Delta E_{\text{opt}}}{\partial B_\theta}, \frac{\partial \Delta E_{\text{opt}}}{\partial B_\phi} = 0$ ), there must also be angles for which  $\Delta E_{\text{opt}}$  is also insensitive

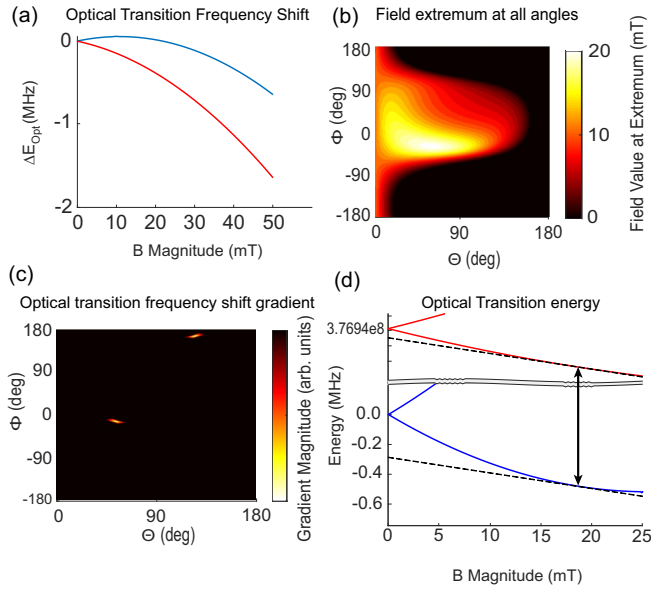


FIG. 5. (a) The shift in the optical transition frequency follows a quadratic dependence with an extrema that, for every orientation, appears at a positive field for the spin conserving  $-1/2 \leftrightarrow -1/2$  transition (blue) and at some negative field for the spin conserving  $+1/2 \leftrightarrow +1/2$  transitions (red). (b) For the  $-1/2 \leftrightarrow -1/2$  spin conserving optical transition and for all angles, the magnetic field value of this extrema is identified. (c) Angular gradient of the optical transition frequency at a field of 19 mT. Two points are visible for which the angular gradient approaches zero. (d) Energy shifts of the two  $-1/2$  spin states at this particular direction vs. magnetic field magnitude. At 19 mT, the slope of the energy change for both states with change in field magnitude is equal (along with the other derivatives) and an optical clock transition occurs.

to first-order angular change to complete each optical clock transition. Though all orientations have some field magnitude that results in an invariant point, only some orientations have angular gradients that simultaneously go to zero. Plotted in Fig. 5(c) is the magnitude of the angular gradient for both spin conserving optical transitions versus the optical transition frequency for all angles of magnetic field with respect to the crystal axes. Two angular points stand out, one for each spin conserving transition, whose gradient value becomes exceedingly small. By cross referencing the points of small angular gradient with the field at which the magnitude extrema appears, we can find an orientation that simultaneously brings all three derivatives to zero. In the case of the spin  $-1/2$  conserving optical transition for “site 1,” we arrive at a set of coordinates  $\vec{B}_{|B|,\theta,\phi} = (19 \text{ mT}, 55^\circ, -15^\circ)$  that correspond to an optical clock transition. The invariant energy levels of this transition at this field are shown in Fig. 5(d). This procedure can be repeated for the remaining sites and potential optical transitions (spin crossing or preserving), giving us the list of optical clock transitions in this material shown in Table II.

Past studies characterize the benefit to coherence gained by using a field invariant direction with the definition of transition curvature given by Ref. [30]. All transitions in Table II share the same curvature of  $\sim 36 \text{ Hz/G}^2$ . Other REIC samples previously brought to invariant points with this magnitude of curvature have resulted in orders of magnitude improvement

TABLE II. Optical clock transitions with angular coordinates of  $\vec{B}$  given relative to the  $\langle 100 \rangle$ ,  $\langle 010 \rangle$ ,  $\langle 001 \rangle$  crystalline axes. These positive and negative projections are based on the unit cell directions for the six sites for the Tm:YGG.

| Site number | $ B $ | $\vec{B}_\theta$ | $\vec{B}_\phi$ | Spin level transition       |
|-------------|-------|------------------|----------------|-----------------------------|
| 1           | 19 mT | $55^\circ$       | $-15^\circ$    | $-1/2 \leftrightarrow -1/2$ |
| 1           | 19 mT | $125^\circ$      | $166^\circ$    | $+1/2 \leftrightarrow +1/2$ |
| 1           | 36 mT | $64^\circ$       | $-150^\circ$   | $+1/2 \leftrightarrow -1/2$ |
| 1           | 36 mT | $117^\circ$      | $31^\circ$     | $-1/2 \leftrightarrow +1/2$ |
| 2           | 19 mT | $54^\circ$       | $76^\circ$     | $-1/2 \leftrightarrow -1/2$ |
| 2           | 19 mT | $125^\circ$      | $-105^\circ$   | $+1/2 \leftrightarrow +1/2$ |
| 2           | 36 mT | $116^\circ$      | $120^\circ$    | $-1/2 \leftrightarrow +1/2$ |
| 2           | 36 mT | $63^\circ$       | $-60^\circ$    | $+1/2 \leftrightarrow -1/2$ |
| 3           | 19 mT | $102^\circ$      | $54^\circ$     | $-1/2 \leftrightarrow -1/2$ |
| 3           | 19 mT | $79^\circ$       | $-127^\circ$   | $+1/2 \leftrightarrow +1/2$ |
| 3           | 36 mT | $64^\circ$       | $120^\circ$    | $+1/2 \leftrightarrow -1/2$ |
| 3           | 36 mT | $118^\circ$      | $60^\circ$     | $-1/2 \leftrightarrow +1/2$ |
| 4           | 19 mT | $38^\circ$       | $20^\circ$     | $-1/2 \leftrightarrow -1/2$ |
| 4           | 19 mT | $143^\circ$      | $-160^\circ$   | $+1/2 \leftrightarrow +1/2$ |
| 4           | 36 mT | $140^\circ$      | $-45^\circ$    | $-1/2 \leftrightarrow +1/2$ |
| 4           | 36 mT | $40^\circ$       | $135^\circ$    | $+1/2 \leftrightarrow -1/2$ |
| 5           | 19 mT | $38^\circ$       | $110^\circ$    | $-1/2 \leftrightarrow -1/2$ |
| 5           | 19 mT | $142^\circ$      | $-70^\circ$    | $+1/2 \leftrightarrow +1/2$ |
| 5           | 36 mT | $140^\circ$      | $45^\circ$     | $-1/2 \leftrightarrow +1/2$ |
| 5           | 19 mT | $40^\circ$       | $-135^\circ$   | $+1/2 \leftrightarrow -1/2$ |
| 6           | 19 mT | $78^\circ$       | $37^\circ$     | $-1/2 \leftrightarrow -1/2$ |
| 6           | 19 mT | $102^\circ$      | $-144^\circ$   | $+1/2 \leftrightarrow +1/2$ |
| 6           | 36 mT | $62^\circ$       | $30^\circ$     | $-1/2 \leftrightarrow +1/2$ |
| 6           | 36 mT | $118^\circ$      | $-150^\circ$   | $+1/2 \leftrightarrow -1/2$ |

to spin coherence times. However, the amount of improvement in the case of Tm:YGG will depend heavily on the decoherence mechanisms involved for this optical transition.

Though the clock transition directions are important for maximizing optical coherence time, alternative crystal properties can also be optimized by choosing other external field directions. Following the arguments from Ref. [34], we have found other orientations that are capable of minimizing the spin inhomogeneous broadening for the ground-state spin transition. Similarly, according to Refs. [22,35] another orientation exists that allows maximizing the branching ratio of the available lambda system in this material. Details on the calculation of these orientations are available in Ref. [23].

## IX. CONCLUSION

We conducted a series of spectroscopic studies that allowed us to measure the full spin-Hamiltonian for Tm:YGG. Despite the multiple sites, a combination of SHB and ODNMR determined both the ground-state and excited-state hyperfine tensors. These tensors were confirmed to match the results of a pair of independent experiments with magnetic field directions limited to the  $\langle 111 \rangle$  crystal axis. This new knowledge allowed us to determine a series of directions that should create optical clock transitions for specific thulium sites, and in turn, enhance the optical coherence of the transition in this material. This confirms the potential of Tm:YGG crystals for quantum networking and quantum memory applications.



## ACKNOWLEDGMENTS

All research at Montana State University was sponsored by Air Force Research Laboratory under Agreement No. FA8750-20-1-1009. Additionally, we acknowledge funding through the Netherlands Organization for Scientific Research

(NWO), and the European Union's Horizon 2020 research and innovation program under Grant Agreement No. 820445 and project name Quantum Internet Alliance. Finally, we appreciate the help of Thomas Rust for his work cutting and polishing some of the many crystal samples used in this work.

- 
- [1] W. R. Babbitt, Z. W. Barber, S. H. Bekker, M. D. Chase, C. Harrington, K. D. Merkel, R. K. Mohan, T. Sharpe, C. R. Stiffler, A. S. Traxinger, and A. J. Woitke, From spectral holeburning memory to spatial-spectral microwave signal processing, *Laser Phys.* **24**, 094002 (2014).
- [2] W. Tittel, M. Afzelius, T. Chanelière, R. Cone, S. Kröll, S. Moiseev, and M. Sellars, Photon-echo quantum memory in solid state systems, *Laser Photonics Rev.* **4**, 244 (2010).
- [3] Y. C. Sun, *Rare Earth Materials in Optical Storage and Data Processing Applications*, edited by R. Hull, J. P. R. M. Osgood, H. Warlimont, G. Liu, and B. Jaquier (Springer Berlin, Heidelberg, 2005), pp. 379–429.
- [4] A. Kaplyanskii and R. McFarlane, *Spectroscopy of Crystals Containing Rare Earth Ions* (Elsevier, Amsterdam, North Holland, 2012).
- [5] E. Fraval, M. J. Sellars, and J. J. Longdell, Method of Extending Hyperfine Coherence Times in  $\text{Pr}^{3+} : \text{Y}_2\text{SiO}_5$ , *Phys. Rev. Lett.* **92**, 077601 (2004).
- [6] R. MacFarlane, C. Yannoni, and R. Shelby, Optical line narrowing by nuclear spin decoupling in  $\text{Pr}^{3+} : \text{LaF}_3$ , *Opt. Commun.* **32**, 101 (1980).
- [7] O. Guillot-Noël, P. Goldner, E. Antic-Fidancev, and J. L. Le Gouët, Analysis of magnetic interactions in rare-earth-doped crystals for quantum manipulation, *Phys. Rev. B* **71**, 174409 (2005).
- [8] N. Ohlsson, M. Nilsson, S. Kröll, and R. K. Mohan, Long-time-storage mechanism for  $\text{tm}:\text{yag}$  in a magnetic field, *Opt. Lett.* **28**, 450 (2003).
- [9] C. W. Thiel, N. Sinclair, W. Tittel, and R. L. Cone, Optical decoherence studies of  $\text{Tm}^{3+} : \text{Y}_3\text{Ga}_5\text{O}_{12}$ , *Phys. Rev. B* **90**, 214301 (2014).
- [10] C. W. Thiel, N. Sinclair, W. Tittel, and R. L. Cone,  $\text{Tm}^{3+} : \text{Y}_3\text{Ga}_5\text{O}_{12}$  Materials for Spectrally Multiplexed Quantum Memories, *Phys. Rev. Lett.* **113**, 160501 (2014).
- [11] M. Zhong, M. P. Hedges, R. L. Ahlefeldt, J. G. Bartholomew, S. E. Beavan, S. M. Wittig, J. J. Longdell, and M. J. Sellars, Optically addressable nuclear spins in a solid with a six-hour coherence time, *Nature (London)* **517**, 177 (2015).
- [12] M. Rančić, M. P. Hedges, R. L. Ahlefeldt, and M. J. Sellars, Coherence time of over a second in a telecom-compatible quantum memory storage material, *Nat. Phys.* **14**, 50 (2018).
- [13] R. Macfarlane and R. Shelby, in *Spectroscopy of Solids Containing Rare Earth Ions*, edited by A. Kaplyanskii and R. Macfarlane, Modern Problems in Condensed Matter Sciences Vol. 21 (Elsevier, Amsterdam, North Holland, 1987), Chap. 3.
- [14] A. Abragam and B. Bleaney, *Electron Paramagnetic Resonance of Transition Ions* (Oxford University Press, Oxford, UK, 2012).
- [15] M. Teplov, Magnetic resonance on  $\text{Pr}^{141}$  nuclei in a  $\text{Pr}_2(\text{SO}_4)_3 \cdot 8\text{H}_2\text{O}$  single crystal, *Zh. Eksp. Teor. Fiz.* **53**, 1510 (1967).
- [16] L. Veissier, C. W. Thiel, T. Lutz, P. E. Barclay, W. Tittel, and R. L. Cone, Quadratic zeeman effect and spin-lattice relaxation of  $\text{Tm}^{3+} : \text{YAG}$  at high magnetic fields, *Phys. Rev. B* **94**, 205133 (2016).
- [17] A. Abragam and B. Bleaney, Enhanced nuclear magnetism: Some novel features and prospective experiments, *Proc. R. Soc. London. Series A: Math. Phys. Sci.* **387**, 1793 (1983).
- [18] J. F. Dillon and L. R. Walker, Ferrimagnetic resonance in rare-earth doped yttrium iron garnet. ii. terbium substitution, *Phys. Rev.* **124**, 1401 (1961).
- [19] G. Menzer, Xx. die kristallstruktur der granate, *Z. Kristallographie - Crystalline Materials* **69**, 1 (1929).
- [20] Y. Sun, G. M. Wang, R. L. Cone, R. W. Equall, and M. J. M. Leask, Symmetry considerations regarding light propagation and light polarization for coherent interactions with ions in crystals, *Phys. Rev. B* **62**, 15443 (2000).
- [21] R. Lauro, T. Chanelière, and J. L. L. Gouët, Slow light using spectral hole burning in a  $\text{Tm}^{3+} : \text{YAG}$  crystal, [arXiv:0902.2657](https://arxiv.org/abs/0902.2657).
- [22] A. Louchet, J. S. Habib, V. Crozatier, I. Lorgeré, F. Goldfarb, F. Bretenaker, J.-L. L. Gouët, O. Guillot-Noël, and P. Goldner, Branching ratio measurement of a  $\Lambda$  system in  $\text{Tm}^{3+} : \text{YAG}$  under a magnetic field, *Phys. Rev. B* **75**, 035131 (2007).
- [23] See Supplemental Material and the references therein at <http://link.aps.org/supplemental/10.1103/PhysRevB.104.134103>, for details on the matching SHB and ODNMR tensor measurements for another set of crystal orientations, further information about the other special directions in the measured tensors, and methods for calculating them.
- [24] L. Erickson, The nuclear quadrupole interaction in  $\text{Pr}^{3+} : \text{LaF}_3$  an optical-rf double resonance measurement of the ground electronic state, *Opt. Commun.* **21**, 147 (1977).
- [25] A. J. Silversmith, A. P. Radliński, and N. B. Manson, Optical study of hyperfine coupling in the  ${}^7\text{F}_0$  and  ${}^5\text{D}_0$  states of two  $\text{Eu}^{3+}$  centers in  $\text{CaF}_2$  and  $\text{CdF}_2$ , *Phys. Rev. B* **34**, 7554 (1986).
- [26] E. Jones, Observation of the  $\text{tm}169$  nuclear magnetic resonance in thulium gallium garnet, *J. Phys. Chem. Solids* **29**, 8 (1968).
- [27] V. H. Schmidt and E. D. Jones, Nuclear-magnetic-resonance study of thulium aluminum garnet, *Phys. Rev. B* **1**, 1978 (1970).
- [28] D. L. McAuslan, J. G. Bartholomew, M. J. Sellars, and J. J. Longdell, Reducing decoherence in optical and spin transitions in rare-earth-metal-ion-doped materials, *Phys. Rev. A* **85**, 032339 (2012).
- [29] J. V. Vleck, *The Theory of Electric and Magnetic Susceptibilities*, Oxford: [s.n.] (Clarendon Press, Oxford, UK, 1932).
- [30] J. J. Longdell, A. L. Alexander, and M. J. Sellars, Characterization of the hyperfine interaction in europium-doped yttrium orthosilicate and europium chloride hexahydrate, *Phys. Rev. B* **74**, 195101 (2006).

- [31] M. Lovrić, P. Glasenapp, D. Suter, B. Tumino, A. Ferrier, P. Goldner, M. Sabooni, L. Rippe, and S. Kröll, Hyperfine characterization and spin coherence lifetime extension in  $\text{Pr}^{3+} : \text{La}_2(\text{WO}_4)_3$ , *Phys. Rev. B* **84**, 104417 (2011).
- [32] D. Kielpinski, V. Meyer, M. A. Rowe, C. A. Sackett, W. M. Itano, C. Monroe, and D. J. Wineland, A decoherence-free quantum memory using trapped ions, *Science* **291**, 5506 (2001).
- [33] R.-C. Tongning, T. Chanelière, J.-L. L. Gouët, and M. F. Pascual-Winter, Optical clock transition in a rare-earth-ion-doped crystal: coherence lifetime extension for quantum storage applications, *J. Phys.: Conference Series* **605**, 012037 (2015).
- [34] M. F. Pascual-Winter, R.-C. Tongning, T. Chanelière, and J.-L. Le Gouët, Spin coherence lifetime extension in  $\text{Tm}^{3+}:\text{YAG}$  through dynamical decoupling, *Phys. Rev. B* **86**, 184301 (2012).
- [35] F. de Seze, A. Louchet, V. Crozatier, I. Lorgéré, F. Bretenaker, J.-L. Le Gouët, O. Guillot-Noël, and P. Goldner, Experimental tailoring of a three-level  $\Lambda$  system in  $\text{Tm}^{3+} : \text{YAG}$ , *Phys. Rev. B* **73**, 085112 (2006).